Journal of Polymer Research (2022) 29: 86
https://doi.org/10.1007/s10965-022-02943-5

ORIGINAL PAPER

Enhancement of physico-chemical, optical, dielectric and antimicrobial properties of polyvinyl alcohol/carboxymethyl cellulose blend films by addition of silver doped hydroxyapatite nanoparticles

Doaa A. Nasrallah[1] · **Manar A. Ibrahim**[1]

Received: 25 October 2021 / Accepted: 8 February 2022 / Published online: 17 February 2022

Abstract
Hydroxyapatite nanoparticles doped with silver AgHA-NPs were synthesized successfully then added with various mass fractions to a mixed solution of polyvinyl alcohol (PVA)/ carboxymethyl cellulose (CMC) using the casting technique. Experimentally, the influence of silver doped hydroxyapatite nanoparticles on the structural, optical, dielectric and antimicrobial properties of nanocomposite films was investigated. X-ray diffraction and Fourier transformation infrared spectroscopy were used to explore the structural features of these films. The XRD analysis revealed the amorphous nature of PVA/CMC blend and the intensity of the characteristic peak of the virgin polymers in the nanocomposite spectrum being much reduced as the doping level was increased. The FT-IR spectra indicated that the blend components were miscible by revealing the functional groups of two polymers that interacted through the formation of a hydrogen bond while, the FT-IR spectra of nanocomposite confirmed the good interaction between the blend chains and AgHA-NPs. The morphological graphs of the prepared blend were formed as hexagonal grains with size distribution around 18.36–24.11 µm. The addition of AgHA-NPs changed the surface morphology of the blend significantly. The optical properties of PVA/ CMC blend and nanocomposites films were measured in the 200–800 nm wavelength range. Optical measurements showed that the optical transmittance for pure blend was nearly 90% while it decreased to 50% with increasing AgHA-NPs contents up to 40 wt.%. The energy gap values calculated by Tauc's model and those determined by ASF model are consistent, where their values reduced by AgHA-NPs incorporation. The dielectric constant of all samples were studied in range of temperatures (303–405 K) and from100 kHz to 1.0 MHz, range of frequencies. The Correlated Barrier Hopping (CBH) is the most appropriate conduction mechanism based on the frequency dependence of the ac conductivity. Silver ion release was examined showed that he film loaded with 10 wt.% AgHA-NPs has a small release of silver ion, while the amount of the Ag^+ released from the samples increased slowly with increasing the content of AgHA-NPs. PVA/CMC/AgHA films were tested for antibacterial activity against both *(Bacillus subtilis*) and *(Escherichia coli*) as well as the anti-fungal activity against (*Candida albicans*),their results showing an increase in the activity index as the filling level of AgHA-NPs increases. The study confirmed that doping of AgHA-NPs into PVA/CMC improves both electrical conductivity and antimicrobial efficiency and these nanocomposites might be recommended for further work in biomedical applications such as wound dressing and infection control.

Keywords PVA/CMC · Hydroxyapatite · UV/Vis. · Dielectric properties · Antimicrobial properties

Introduction

Polymer nanocomposites are one of the most important materials in the academic and industrial areas, and are produced by dispersing nanofillers with one or more dimensions at nano-scale into the polymeric matrix [1]. Recently, researchers have been attracted to polymer nanocomposites over conventional microcomposites due to their wide applications in electromechanical systems and their large interfacial area per unit volume of the dispersion medium [2]. The integration of the properties of these components (polymer and nanoparticles) can result in a material with enhanced optical, electrical, mechanical and antimicrobial properties. Nanocomposites with antibacterial properties can

✉ Doaa A. Nasrallah
doaa582012@gmail.com

[1] Physics Department, Faculty of Science, Zagazig University, Zagazig, Egypt

be acquired either by incorporating nanoparticles that have a recognized antibacterial activity, or by improving the antibacterial characteristics of the polymeric matrix [3].

Currently, the scientists are looking towards developing new bioactive compounds with silver at a nanometric scale. The research interest in this field of materials science is to find an suitable biomaterial and successfully incorporate silver ions. Hydroxyapatite (HA) is one of the most representative biomaterials that based on calcium phosphate as calcium is an important secondary messenger that plays a role in a number of wound-healing signalling pathways. HA has been extensively studied for its bone regeneration and bone-engineering applications, due to its analogous molecular composition to human bone [4]. Lately, the development of composite membranes and polymeric films based on hydroxyapatite (HA) has been seen, owing to their possibility applications in orthopedics [5]. It is greatlyaccepted that substituting a small quantity of Ca^{2+} ions in the HA structure can cause lattice disorder, reduction in particle size, decrease in the degree of crystallinity and an increment in bioresorption [6]. Multiple studies have shown that, incorporation of Eu, Ag, Cu, Zn, Ce, and Nd ions in HA structure can influence its physical, chemical and biological properties where existance of dopant in HA structure can lead to increased release of Ca^{2+} ions in surrounding fluid, which can induce rapid deposition of apatite on the template's surface. It was reported that Ce^{3+} doped HA can increase the HA solubility, which could lead to improved biodegradability and antibacterial properties [7]. While, Substitution of Nd^{3+} into HA lattice promotes the healing of bone fractures because its good electrical conductivity [8]. Whilst, Eu^{3+} doped HA is a good drug carrier, which can be easily tracked in vivo due to its strong photoluminescence emission [9]. It is thought the doping of HA with silver nanoparticles (AgNPs) may improve the biological characteristics of HA, where silver and silver-based materials have been utilized since ancient times for wound disinfection and also in the treatment of microbial infections [10]. Silver exhibits good thermal stability, low volatility, is biocompatible and non–toxic to human cells at low concentrations along with excellent antibacterial properties [11]. A lot of the regard in development of nanocomposites for healing and wound-dressing applications stems from the specific features of nanofillers themselves. Recent advancements in effective antimicrobial wound dressing incorporating silver nanoparticles have stimulated a deeper search for development of such composites for improved wound healing [12–15].

Biocompatible and bioresorbable polymers are usually utilized among the most commonly used polymers for obtaining the aforementioned composites because of their ability to be desorbed into the human body over time and to encourage osteoblast proliferation during bone implant. Consequently, the development of biopolymers-based biocomposite consisting of biopolymers strengthened with ceramic inorganic micro-/nanofillers has a large importance in the bone tissue regeneration research [16]. Among biopolymers, the semicrystalline PVA and amorphous CMC are hydrophilic, non-toxic and biodegradable. Moreover, these polymers have the capability to form excellent flexible-type films using solution casting technique [17]. The cross-linked polyvinyl alcohol (PVA, CH2CHOH) is a helpful material for a broad range of applications particularly in the fields of medicine and pharmaceutical science [18]. Owing to good characteristics such as biocompatibility, chemical resistance, and many intriguing physical properties that are employed for different applications, polyvinyl alcohol (PVA) is currently trending as a candidate of synthetic articular cartilage. PVA is a promising material with great storage capacity, dielectric strength, and electrical characteristics [19]. Otherwise, one of the important cellulose derivatives, Carboxymethyl cellulose (CMC),is usually prepared through the reaction of alkali cellulose with monochloroacetate or its sodium salt in organic medium. CMC has many desired properties, such as filming, emulsification, suspension and water retention. As a result, it is utilized in various applications like food science as a viscosity modifier or thickener and to stabilize emulsions in many products such as ice cream. Also, It is a constituent of various nonfood products, including toothpaste, detergents, water-based paints, textile sizing, electrical elements and a variety of paper products [20]. Due to the existence of the hydroxyl group (OH) inside the chain backbone of PVA and CMC structures, stronger inter- and intra- hydrogen bonding can be produced. In recent years, research on PVA and Carboxylmethylcellulose sodium CMC blend films has been a popular topic [21].

Novel composite films based on PVA/CMC/silver doped hydroxyapatite NPs have been prepared, in order to produce nanocomposite films with enhanced optical and electrical properties. The current study presents a simple method to prepare compact PVA/CMC/AgHA composite films by dispersing different concentrations of HA nanoparticles doped with Ag + ions in the blend solution. These films were characterized microstructurally using FTIR and XRD; where as its morphology was assessed using SEM. They were also evaluated for optical and dielectric analysis. Antimicrobial activity of the samples was also studied.

Experimental procedures

Materials

CMC powder, El Nasr Pharmaceutical Chemicals Co., Cairo, Egypt and PVA grains (M.W. $\approx 4 \times 10^4$ g/mol) Alfa Aesar–Karlsruhe–Germany were used to form the blend sample. The double distilled water (DD), from

Al-Gomhoria Company, Cairo, Egypt, was utilized as a solvent for the polymeric materials. Calcium nitrate tetrahydrate [$Ca(NO_3)_2{\cdot}4H_2O$] and di-ammonium hydrogen orthophosphate [$(NH_4)_2HPO_4$] were purchased from Loba Chemie, Colaba, Mumbai (India), silver nitrate ($AgNO_3$) was purchased from Alfa Aesar–Karlsruhe–Germany to be used as a raw material for the preparation of the silver doped hydroxapatite NPs.

Preparation of the silver doped hydroxapatite NPs

Silver doped hydroxyapatite nanoparticles AgHA-NPs was synthesized by solution-precipitation method using calcium nitrate tetrahydrate [$Ca(NO_3)_2{\cdot}4H_2O$], di-ammonium hydrogen orthophosphate [$(NH_4)_2HPO_4$] and silver nitrate ($AgNO_3$) as sources of calcium (Ca), phosphorous (P) and silver (Ag) ions, respectively. The $Ca_{10-x}\ Ag_x\ (PO_4)_6\ (OH)_2$ [Ag doped HA], with $x_{Ag}=0.5$ was prepared by replacing Ca with Ag (x = 0.5) and keeping the molar ratio [Ca + Ag]:P to 1.67. Calcium and silver nitrate solution was formed by dissolving a required amount in 250 ml of distilled water to prepare [Ca + Ag] molar solution. Subsequently, 0.6 M phosphate solution produced in distilled water was added drop by drop to [Ca + Ag] solution at 70 °C on a hot plate with vigorous stirring. The pH of the solution was kept at 10 by adding ammonium hydroxide. The solution left under stirring for two hours until white Ag doped HA precipitates formed. The obtained suspension was aged for one day at room temperature. After that, the filtered AgHA precipitates were washed with distilled water and left to dry in a furnace at 100 ºC. Finally, the obtained white powders were grounded to fine particles.

Preparation of PVA/CMC/AgHA nanocomposite samples

Pure PVA/CMC and its nanocomposite films were prepared by conventional solution cast technique. Firstly, 2 gm of (polyvinyl alcohol and carboxyl methyl cellulose) were dissolved in100 ml of the double distilled water (DD) in two distinct flasks with constant stirring at 40°C for 4 h. Then, the two polymer solutions were added together for 6 h to obtain more homogeneous PVA/CMC solution with (50/50 wt. %). PVA/CMC/AgHA nanocomposite films were prepared by adding different proportions of AgHA-NPs (10, 20, 30, 40 wt. %) to the previously prepared blend solution. After stirring for another 8 h, the mixture had turned turbid and milky white and then poured into glass petri dishes and left to dry in an oven at 50 °C for 24 h. Finally, the films were carefully removed from the petri dishes. The thickness of the films was measured with the use of a digital micrometer with accuracy ± 0.001 mm and given as the mean values of five random points for each sample.

Techniques used for samples characterization

To investigate the crystalline structures of the prepared nanocomposite samples PVA/CMC/AgHA, Philips X-ray diffractometer, with a Cu $K\alpha$ source of λ = 1.54 A° was used to obtain the XRD spectra in the range 5–70°.The interactions between PVA/CMC and (AgHA) NPs were examined using Fourier transform infrared spectroscopy (pruker vertex 70) in the wavenumber range (4000–400 cm^{-1}). Scanning electron microscope (SEM),(JEOLJSM 6510 LV, USA)was used to examine the morphological properties at an accelerating voltage of 30 kV. The surface was coated with 4 nm thick gold layer to reduce the charging e-beam effects. The optical properties were studied using an ultraviolet/visible spectrophotometer (UV/Vis., V-570 UV/VIS/NIR, JASCO, Japan) at room temperature in the wavelength range 200–800 nm. The ac conductivity and dielectric parameters of the synthesized films were investigated using an automatic programming RLC meter (FLUKE PM6306) at the frequencies ranging from 100 Hz to 1 MHz, and in the temperature ranges between 303 and 373 K at approximately 10 K intervals. The AC conduc-tivity σ was estimated from the relation:

$$\sigma(w) = \frac{d}{RA} = \sigma_{AC} + \sigma_{DC} \tag{1}$$

where d (cm) is the thickness of the sample, R is the resistance and A represents the cross-section area. The σ_{AC} is the electrical conductivity, ω is the angular frequency ($\omega = 2\pi f$) and σ_{DC} is the DC conductivity. The dielectric constant ε' was obtained from [22]:

$$\varepsilon' = \frac{C.d}{\varepsilon_0 A} \tag{2}$$

where C is the capacitance and $\varepsilon_O = 8.85 \times 10^{-12} Fm^{-1}$. The silver coated disk-shaped samples were placed between two polished brass electrodes to directly measure the capacitance C_P and the resistance R_P in parallel.

Silver ion release test

The prepared films were cut into small equal size. Then the films were immersed into a sterilized plastic container including 30 ml of phosphate buffer solution (pH 7.4), and incubated at 37 °C for 24 h. The silver ion concentrations in the solutions were then measured by Agilent 5100 Inductively Coupled Plasm –Optical Emission Spectrometer (ICP-OES) with Synchronous Vertical Dual View (SVDV). The number of samples (n = 3) for each concentration and the average value of the silver ion concentrations was taken to confirm the results.

Antimicrobial evaluation

The anti-microbial activity of the prepared films was examined against gram positive bacteria (*Bacillus subtilis*) and Gram-negative bacteria (*Escherichia coli*) as well as the anti-fungal activity was tested against (*Candida albicans*). Sample of each film was dissolved in DMSO and then prepared a solution of 1 mg /ml concentration separately. Whitman filter paper discs of standard size (5 cm) were made, cut and sterilized in an autoclave. The paper discs were placed aseptically in the petri dishes containing nutrient agar media (agar 20 g + beef extract 3 g + peptone 5 g) loaded with *Bacillus subtilis, E. coli and Candida albicans* after being soaked in the necessary concentration of the complex solution. The inhibitory zones were measured after 24 h of incubation of petri dishes at 36 C°. Each procedure was carried out three times. The percent activity index for the samples was estimated by the formula as follow:

$$\%\,\textbf{Activity Index} = \frac{\textbf{Inhibition zone by test compound (diametre)}}{\textbf{Inhibition zone by standard (diametre)}} \times 100$$

Results and discussion

X-ray diffraction analysis (XRD)

The patterns of X-ray diffraction were investigated in the range of 2θ between 4° and 70°. Figure 1a demonstrates the XRD pattern of AgHA-NPs, the peaks identified at 2θ = 25.85 °, 28.97 °, 31.79 °, 32.15 °, 32.92 °, 46.72 °, 49.47 ° and 53.14° corresponds to the diffraction planes (002), (012), (121), (112), (030), (222), (123) and (004), respectively. The diffraction peaks of AgHA-NPs can be well indexed to hexagonal crystalline hydroxyapatite in P63/m space group (ICDD card No.00–064-0738). The absence of any secondary phase implies that silver ions have successfully replaced calcium ions in hydroxyapatite crystal structure without causing any disruption. This finding is consistent with earlier studies [23, 24]. Figure 1b reveals XRD patterns of virgin blend and blend filled with different amounts of AgHA-NPs. It can be observed that the pure PVA/CMC matrix and loading AgHA-NPs films have a broad peak around 2θ = 20° which attributed to the amorphous nature of the PVA and CMC. Also, it could be inferred that the intensity of this peak decreases upon the addition of AgHA-NPs. The changes might be due to the interaction that occurred between the host polymer blend and AgHA-NPs. Additionally, the more inter- and intra-molecular attraction could take place and in turn soften the polymer backbone. Moreover, it has to be distinguished that the XRD of the prepared PVA/CMC/AgHA nanocomposites exhibited the existence of AgHA-NPs within the polymeric matrix as shown in Fig. 1b, confirmed the well formation of nanocomposite. Correspondingly, the intensity of AgHA-NPs peaks in the prepared nanocomposite increases with rising the percentage of AgHA-NPs in the polymeric matrix.

Scherrer's equation was used to compute the average crystallite size of the AgHA-NPs and nanocomposites.

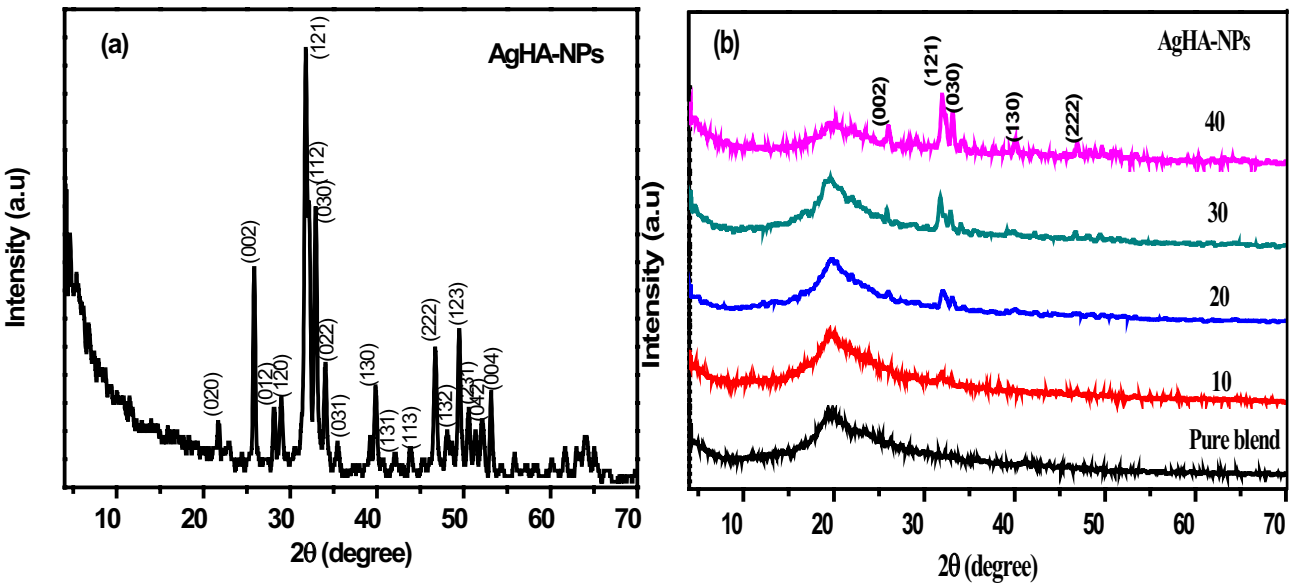

Fig. 1 (**a**) X-ray diffraction pattern of AgHA-NPs, (**b**) X-ray diffraction pattern of PVA/CMC nanocomposites incorporated with different concentrations of AgHA-NPs (0, 10, 20, 30 and 40 wt.%)

$$D = k\lambda/\beta cos(\theta) \quad (3)$$

where, λ express X-ray wavelength (0.154056 nm), θ is the Bragg angle, β represents the full width at half maximum (FWHM) intensity of the high intensity peak (radians) and k is constant related to the crystallite shape (K ≈ 1). The average calculated crystallite size of synthesized AgHA nanoparticles was found to be 25.88 nm. On the other hand, the average values of crystallite sizes of PVA/CMC/AgHA nanocomposites lie in the range of 11.7–14. 5 nm. This size is very close to the value of 18.6–16.4 nm for bone apatite.

The crystallinity (X_c) of the crystalline phase was determined according to the following equation [25]:

$$X_c = (K_A/\beta_{1/2})^3 \quad (4)$$

where K_A is a constant set at 0.24 and $\beta_{1/2}$ is the FWHM of the (002) reflection (in degrees). The crystallinity of AgHA nanoparticles was 1.728, however the cystallinity of AgHA-NPs decreases as they were incorporated into the PVA/CMC matrix then increases with increasing the AgHA-NPs content. The cystallinity of AgHA-NP in the composites ranging from 0.884 to 1. The increasing of the AgHA-NPs content provoked a decrease in the broadening of the diffraction peak (002) as shown in Fig. 1b, as it is noticeable in crystallinity (X_c) increases.

Fourier transform infrared spectroscopy (FTIR) analysis

Figure 2 shows the FTIR spectra of pure PVA/CMC blend and blend filled with various concentrations (10, 20, 30, 40 wt. %) of AgHA-NPs. FTIR spectrum of PVA/CMC blend reveals the major characteristics bands for the virgin polymers PVA and CMC. The broad bands at 3282 cm^{-1} and 2920 cm^{-1} could be assigned to the O–H stretching vibrational mode and C–H starching vibration, respectively. The observed band at 1594 cm^{-1} is ascribed to carboxyl group´s asymmetric vibrational mode, whereas the existence of CH_2 and C–O bending is shown by the bands around 1416 and 1322 cm^{-1}, respectively. Furthermore, the band at 1048 cm^{-1} is from stretching of C–O while, the band at 843 cm^{-1} is due to the rocking of CH_2. According to Saadiah et al. [26], the development of intermolecular forces of H-bonding between the PVA and CMC of the blend is expected, and these take place at the bending –OH region and asymmetric $–COO^-$ functional group. From the FTIR spectra for PVA/CMC/AgHA films, the incorporation of AgHA-NPs influences the functional groups for PVA/CMC matrices as a result of interactions between these groups and AgHA-NPs. As shown in Fig. 2, the intensity of OH stretching vibration band of pure blend at 3282 cm^{-1} decreased and slightly shifted to lower wave number (blue shift) with the addition of AgHA-NPs. The intensity of C = O band

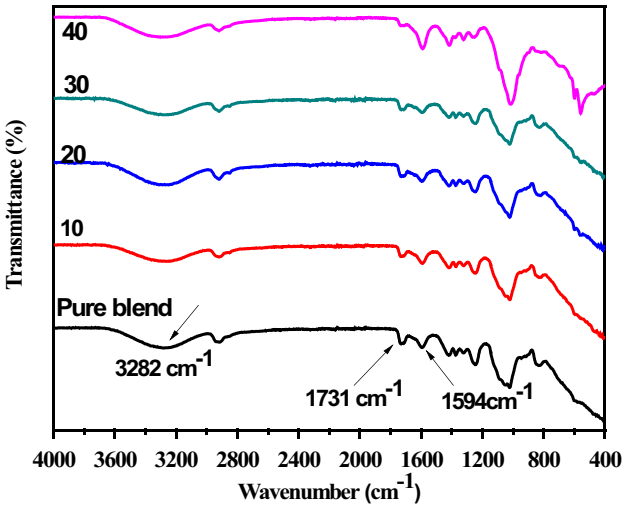

Fig. 2 FT-IR spectra of pure PVA/CMC polymeric blend and filled with different concentrations of AgHA-NPs (0, 10, 20, 30 and 40 wt.%)

at 1731 cm^{-1} of PVA gradually decreased with increasing AgHA-NPs content. The intensity of COO^- band of CMC increased and moved toward lower wave number than that of pure blend, exhibiting a shift from 1594 cm^{-1} to 1584 cm^{-1}. Also, it can be observed an increment in the intensity of the band at 1022 cm^{-1} with increasing the content of AgHA-NPs. Furthermore, at a high concentration of AgHA NPs (40 wt.%), it is noticed a band at 558–604 cm^{-1} which appears as a doublet and attributed to the PO_4^{3-} bending mode of AgHA-NPs. All this finding supports the establishment of hydrogen bond between AgHA-NPs and the pristine PVA/CMC and provide important structural modification information [27].

Morphological features

The scanning electron microscopy (SEM) is a practical method to observe the miscibility of the prepared samples. Figure 3a–e depicts the surface morphology of the PVA/CMC doped with various amounts of AgHA-NPs at magnifications 1500 times. It is possible to notice that the neat polymeric blend of PVA/CMC film was constructed as hexagonal grains with size distribution around 18.36–24.11 µm [28]. Miscibility of PVA and CMC components (in the blend) is confirmed by a uniform and homogeneous smooth surface. As shown in Fig. 3b–e, adding AgHA-NPs causes a significant change in the surface morphology of PVA/CMC matrix in the form of rising the surface roughness as the nanofiller concentration is increased. From Fig. 3 b, c, the grains seem to be decorated with spherical particles. These particles assigned to the presence of AgHA-NPs, which are uniformly distributed in the form of bright spots with

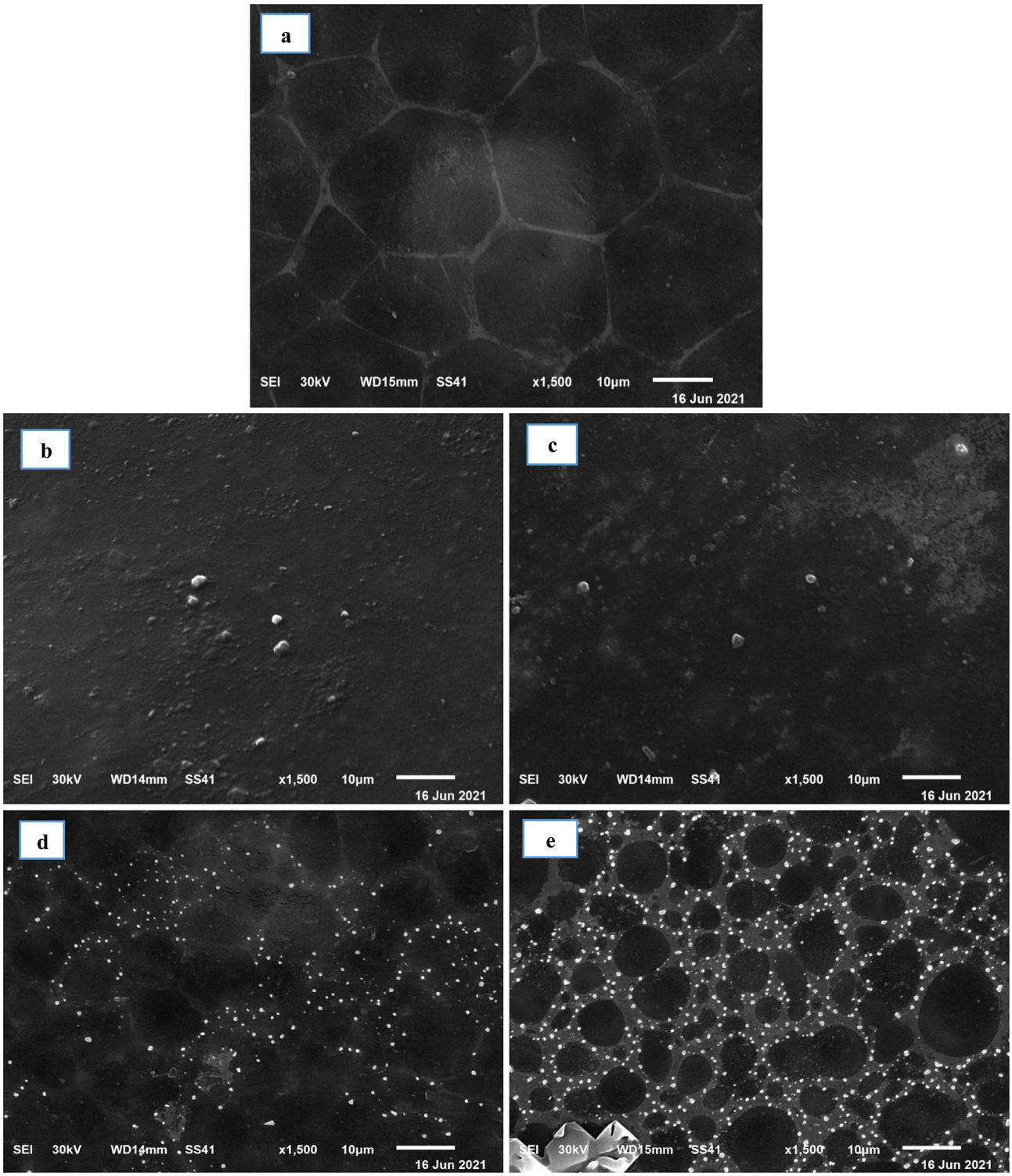

Fig. 3 (**a**-**e**): SEM micrograph for PVA/CMC polymeric blend and filled with different concentrations of AgHA-NPs (0, 10, 20, 30 and 40 wt.%)

no aggregation [29]. By noticing Fig. 3d, e, AgHA-NPs are accumulated among grains boundaries, which can be interpreted by assuming that boundaries have more energy than grains'bulk, and therefore attract towards additional particles. The agglomeration of AgHA-NPs across boundaries may strengthen the connection mechanism among neighboring grains [28]. Because the PVA/CMC blend was loaded with varied quantities of (AgHA) nanoparticles, the

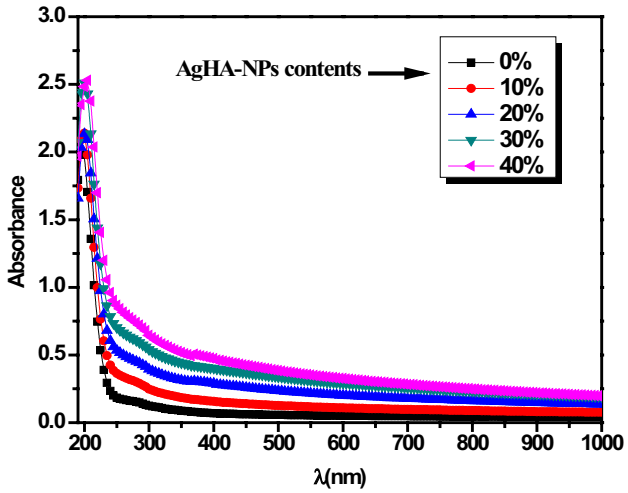

Fig. 4 UV/Vis. Absorbance spectra of PVA/CMC loaded with (0, 10, 20, 30 and 40 wt.% AgHA-NPs)

PVA/CMC/AgHA nanocomposites were undergoing slight destruction throughout the swelling of grains boundary in a non-uniform manner. It can be concluded that, the morphological changes in the neat polymeric blend revealed nanoparticle-polymer interaction indicating that inorganic and organic components within the nanocomposite samples are compatible.

Optical properties

UV–visible spectral analysis

Figure 4 displays the UV–Visible absorption spectra in the wavelength range (200–800 nm) for pure PVA/CMC blend as well as PVA/CMC polymeric films containing various concentrations (10, 20, 30 and 40 wt.%) of silver doped hydroxyapatite nanoparticles (AgHA-NPs). The spectra of pristine PVA/CMC blend has an absorbance band at about 195 nm which is assigned to the $n \rightarrow \pi^*$ transition of C=O [17].The intensity of this band gradually increases with the continuous increase of AgHA-NPs contents in the samples due to high absorbance of AgHA-NPs. It was also noted that, the narrow size distribution of the AgHA-NPs in the polymer matrix leads to symmetric and narrow absorption band. This enhancement in absorbance of the filled samples is due to the agglomeration of AgHA-NPs, which scatter the light, and enhance the absorption coefficient of the nanocomposite samples. This manner of absorbance behavior of these spectra of the nanocomposite samples implies a change in their optical energy band gap with a change in the embedded AgHA-NPs contents and also displays AgHA-NPs complexation with the functional groups of PVA and CMC structures which is confirmed by FTIR analysis. These results suggest that adding AgHA-NPs to PVA/CMC blend modify its optical properties.

Figure 5a, b show the dependence of percentage transmittance (T%) on the wavelength and opacity at 600 nm for undoped blend and nanocomposite films of thickness 0.241 ± 0.010.mm. The opacity of the films was calculated based on Eq. (5) [30]:

$$Opacity = \frac{A_{600}}{X} \tag{5}$$

where, the absorbance value at 600 nm is A_{600} and the film thickness (mm) is X. A greater value of opacity means a smaller transparency of a film. It was observed that, the optical transmittance was increased with wavelength for all samples. In addition, the optical transmittance for

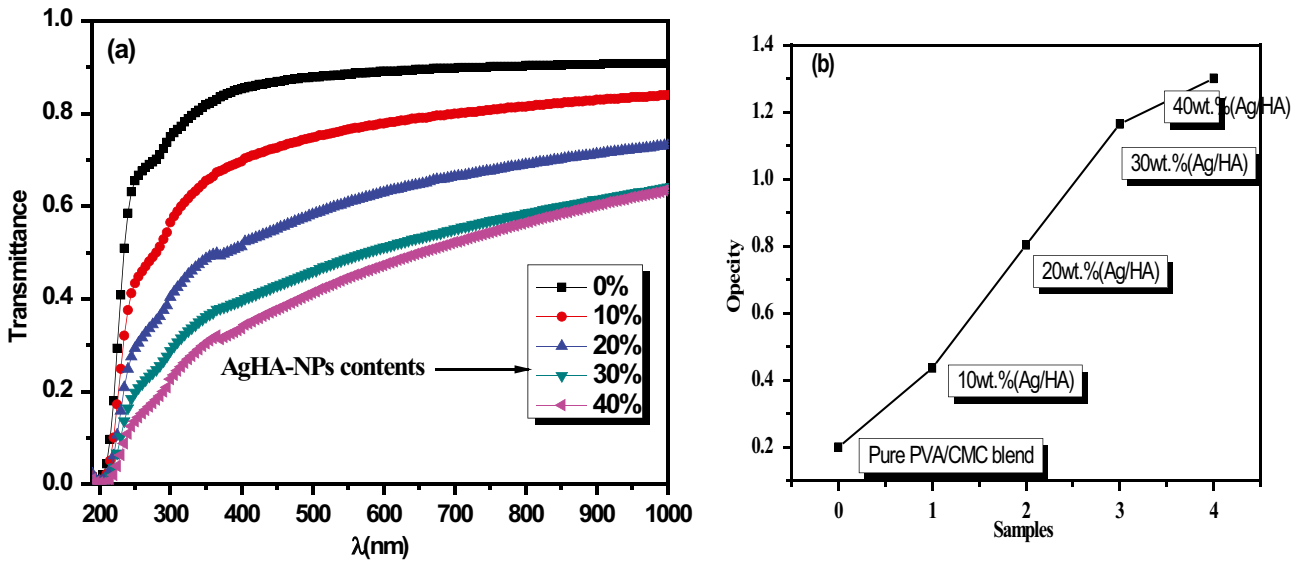

Fig. 5 (**a**) UV/Vis-Transmittance spectra for PVA/CMC loaded with (0, 10, 20, 30 and 40 wt.% AgHA-NPs), (**b**) opacity of samples

pure blend was nearly 90% while it decreased to 50% with increasing AgHA-NPs contents up to 40 wt.%. This can be observed from a simple visual examination of the prepared films as their color gradually transforms from transparent to relatively white, where the PVA/CMC blend film was more transparent (lower opacity value) than films incorporated with AgHA-NPs. On the other hand, the percentage of light transmittance at the wavelengths of 300 and 600 nm are tabulated in Table 1. It was noticed that, filling the PVA/CMC blend with AgHA-NPs results in a drop in T percent to about 22.699% and 47.351% at λ = 300 nm and 600 nm, respectively. Thus, AgHA-NPs included into the blend matrix may behave as scattering centers leading to the observed decrement in T% [31].The results showed that inclusion of AgHA-NPs resulted in a considerable reduction in light transmission in both UV and visible regions. It is worth mentioning that, the effect of AgHA-NPs incorporation was stronger in the UV range than in visible range, implying that the UV barrier properties of film were improved with a reduced influence on its transparency. Because UV ray has a high oxidizing property and can cause deteriorative impact on food products, thus blocking UV ray plays a significant role in food pack ageing industry and has resulted in an increase in food product shelf life [32].

The fundamental absorption edge and optical gap

Determining the band gap value of amorphous materials such as polymers, is crucial in their applications. The most popular method for stimulating the band gap of amorphous materials is to use optical absorption coefficient measurements to establish the fundamental absorption edge that related to the gap. For exact estimation of the absorption edge, the absorption coefficient of the prepared samples was determined using the obtained absorbance (A) according to the equation [33]:

$$\propto = \frac{2.303A}{d(m)} \tag{6}$$

where d is the film thickness. The fluctuation in the absorption coefficient with incident photon energy for pristine as well as doped PVA/CMC blend films is shown in Fig. 6. As observed, the pristine blend films exhibit significant absorption in the UV spectral range indicating a high degree of amorphousity in the films [34]. The position of absorption edge for all prepared samples was determined by plotting the absorption coefficient (α) versus photon energy ($h\upsilon$), as seen in Fig. 6. Extrapolating the linear absorption part of the graphs to the energy axis of the plot yielded the absorption edge (E_e) value. The plot show a progressive red shift in (E_e) values from 2.252 to 1.168 eV by raising the AgHA-NPs levels in the PVA/CMC matrix as tabulated in Table1. The absorption edge shift in the UV region is interpreted by changes in the electron hole in the conduction and valence bands [35]. This result predicts with the decrease in the optical band-gap for the nanocomposites films.

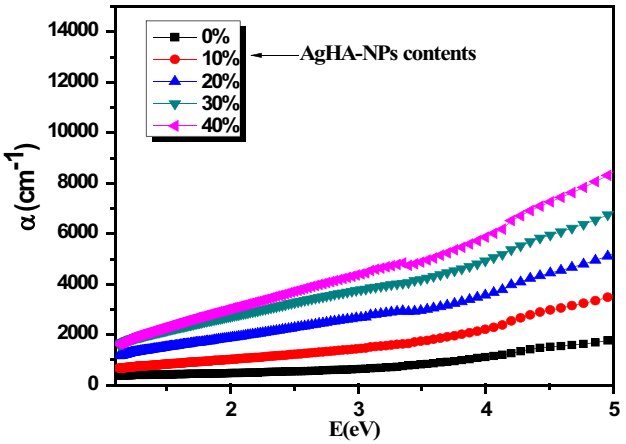

Fig. 6 Absorption coefficient (α) spectra for PVA/CMC loaded with (0, 10, 20, 30 and 40 wt.% AgHA-NPs)

As previously mentioned, determining the optical energy gap is essential for controling the material application in optical and electrical technologies. Indeed, according to Mott and Davis [36, 37], the optical gap E_g^{Opt} for non-crystalline materials can be evaluated using the relation:

$$(\alpha h\upsilon)^n = \beta(h\upsilon - E_g) \tag{7}$$

where, α is the absorption coefficient, $h\upsilon$ is the photon energy, β is a constant and n is the index number differs

Table 1 Percentage transmittance T%, fundamental absorption edge E_e and optical energy gap E_g for pure blend PVA/CMC sample and its filled samples with different concentrations of AgHA- NPs

PVA/CMC blend loaded with AgHA-NPs (wt.%)	T% at 300 nm	T% at 600 nm	E_e (eV)	Indirect E_g^T (eV)	Direct E_g^T (eV)	$_g\lambda$ (nm)	$E_g^{(ASF)}$ (eV)
0	**74.989**	**89.125**	**2.252**	**4.819**	**5.595**	**254**	**4.887**
10	**56.494**	**77.804**	**2.157**	**4.692**	**5.538**	**262**	**4.722**
20	**40.365**	**62.951**	**1.785**	**4.466**	**5.487**	**272**	**4.563**
30	**28.84**	**51.168**	**1.379**	**4.311**	**5.639**	**284**	**4.351**
40	**22.699**	**47.351**	**1.168**	**4.015**	**5.245**	**295**	**4.175**

according to the type of electronic transition. For E_g^{Opt} calculations, value of 'n' is taken equal to 1/2 for indirect and 2 for direct allowed transitions. Figure 7a, b show the $(\alpha h\nu)^{1/2}$ and $(\alpha h\nu)^2$ versus $h\nu$ for PVA/CMC before and after being doped with AgHA-NPs. The $E_g^{(T)}$ values for indirect and direct transitions are obtained by extrapolating the linear part of these plots to zero absorbance. An alternative method based on the absorption spectra fitting model (ASF) can be used to determine the optical band gap by measuring the optical absorbance $A(\lambda)$ without having to measure the film thickness via the relation [38]:

$$A(\lambda) = D\lambda\left(\frac{1}{\lambda} - \frac{1}{\lambda_g}\right)^m \tag{8}$$

where $D = \left[\frac{\beta(hc)^{m-1}d}{2.303}\right]$ and λ_g is the wavelength corresponding to the optical gap $\left(E_g^{(ASF)}\right)$. For indirect transition, the value of λ_g can be evaluated from extrapolation of the linear part of $A^{1/2}/\lambda$ versus $(1/\lambda)$ as seen in Fig. 8. By using the estimated values ofλ_g, the optical band gap ($E_g^{(ASF)}$ (in eV) can be determined as $E_g^{(ASF)} = \frac{1240.5}{\lambda_g(nm)}$.

The fundamental absorption edge (E_e), the estimated indirect and direct optical gap $E_g^{(T)}$ based on Tauc's relation and the optical gap $E_g^{(ASF)}$ calculated by the ASF model are listed in Table 1. The obtained $E_g^{(T)}$ value for pure PVA/CMC is consistent with previously published values [31]. By increasing AgHA-NPs content, all of these values are fall significantly where the values of $E_g^{(T)}$ and $E_g^{(ASF)}$ are nearly equal. The addition of AgHA-NPs with comparatively low energy band gap (~5.26 eV) into the high energy band gap PVA/CMC blend matrix is predicted to result in this reduction. Furthermore, this decrease can be understood in terms of the formation of hydrogen bond between AgHA-NPs and the pure PVA/CMC blend as explained previously in FTIR part. Also, the decrease in E_g of PVA/CMC films with increasing AgHA-NPs content may be attributed to the creation of localized states in the band gap of host PVA/CMC matrix which acts as tapping and recombination center [39].

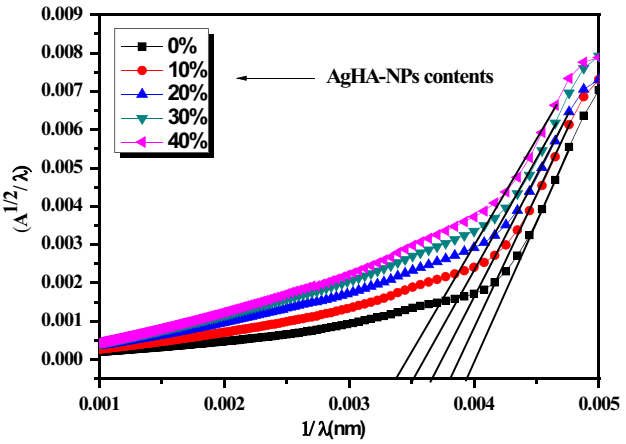

Fig. 8 The relation between $A^{1/2}/\lambda$ versus $(1/\lambda)$ for estimating E_g by ASF model for all the prepared samples

Refractive index and extinction coefficient evaluation

The refractive index (n) is extremely essential in optical communication and optical device design. The most popular approach for calculating the refractive index (n) is the use of reflectance (R) spectra which is related to n by the following relation

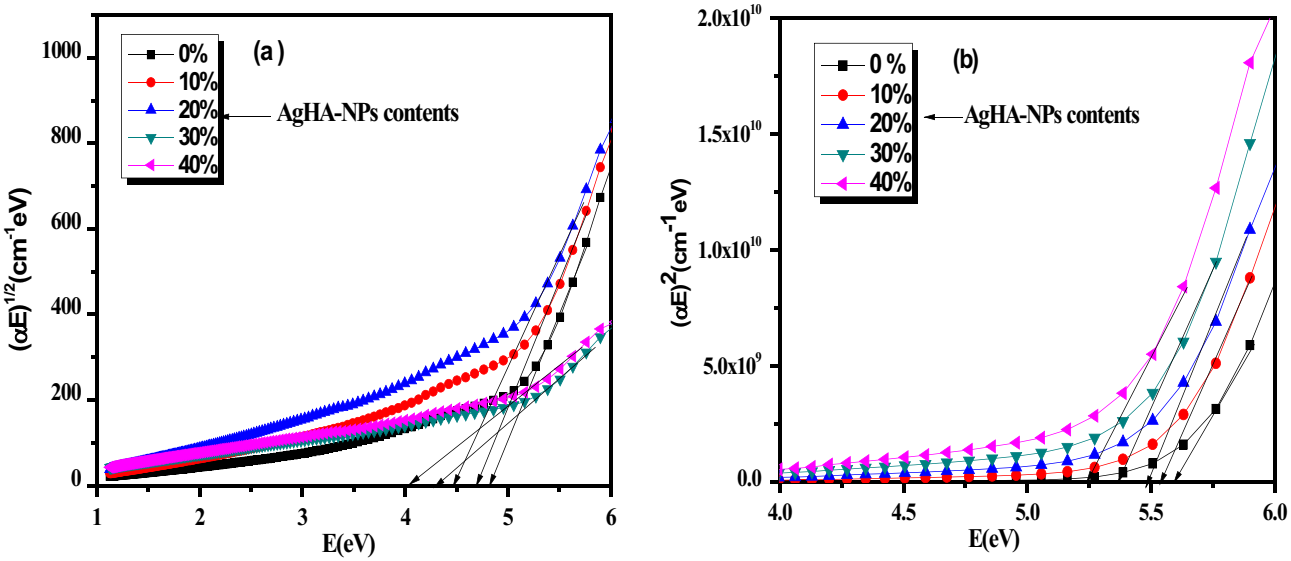

Fig. 7 Tauc's plot: (**a**) $(\alpha h\nu)^{1/2} vs. h\nu$ (the indirect optical band gap), (**b**) $(\alpha h\nu)^2 vs. h\nu$ (the direct optical band gap) for PVA/CMC blend loaded with (0, 10, 20, 30 and 40 wt.% AgHA-NPs)

$$n = \frac{1+\sqrt{R}}{1-\sqrt{R}} \tag{9}$$

Figure 9 shows the dependence of n on the wavelength (λ). In most of the investigated range of λ, the values of n dramatically decrease with λ increment from 275 to 450 nm, then drop slightly but increase with increasing AgHA-NPs content in the blend films, where the intermolecular hydrogen bonding between AgHA nanoparticles and the adjacent OH groups of the polymer blend is thought to be responsible for this behavior leading to increasing the density of the films, and thus the films became more packing [40]. Also increasing the refractive index with raising the doping ratio of AgHA-NPs in the virgin blend can be interpreted by increasing the roughness of the doped films where AgHA-NPs agglomerate on the surface as indicated in SEM graphs.

One of the most important optical characteristics that reflects changes in the material absorption when exposed to electromagnetic radiation is the extinction coefficient (k). The following equation gives (k) coefficient [41]:

$$k = \frac{\alpha\lambda}{4\pi} \tag{10}$$

The extinction coefficient of PVA/CMC/AgHA nanocomposites as well as pure blend varies with photon wavelength as shown in Fig. (10). The extinction coefficient of PVA/CMC blend rises as the concentration of AgHA-NPs rises. The rising number of charge carriers as a result of the increase in the absorption coefficient can explain this behavior of extinction coefficient. In addition, the loss in incident photon energy due to the interaction between the energy carries in the samples and the incident light, which

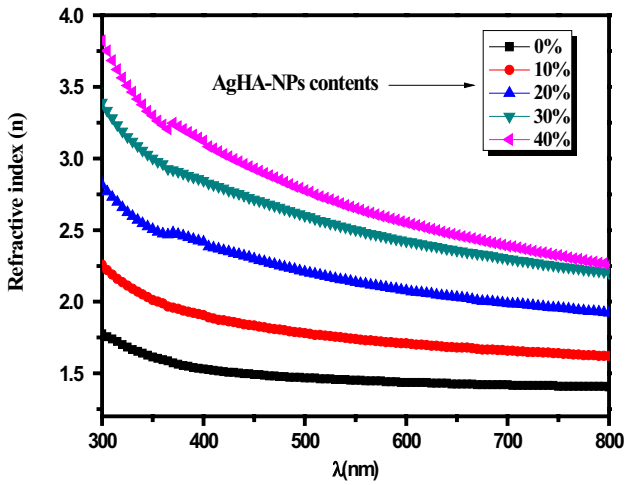

Fig. 9 Variation of Refractive index for pure PVA/CMC blend and PVA/CMC/AgHA nanocomposites with wavelength

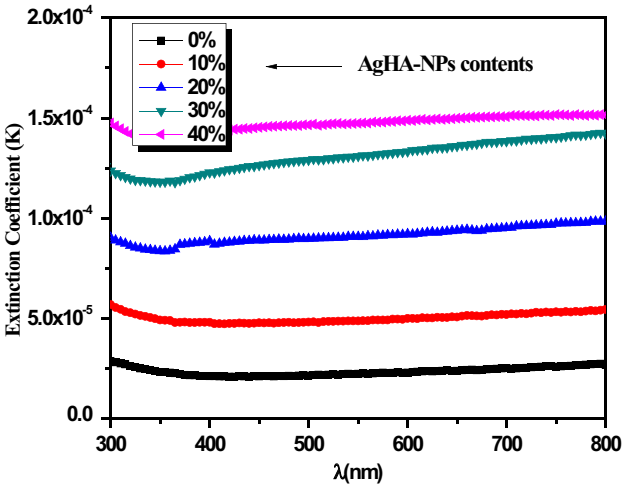

Fig. 10 Variation of extinction coefficient for pure PVA/CMC blend and PVA/CMC/AgHA nanocomposites with wavelength

leads to polarize of the medium charges. This result indicates that AgHA-NPs will modify the structure of the host PVA/CMC matrix blend.

Dielectric characterization

Dielectric constant

Figure 11 shows the dependence of dielectric constant ε' of PVA/CMC blend, and blend loaded with (10, 20, 30, 40 wt.%) AgHA-NPs at different temperatures. The plot of ε′ is systematically decreases with incremental frequency over the studied frequency range (100 Hz-1 MHz). These graphs show that at low frequency and high temperatures, the dielectric constant values are extremely high. The large observed values of ε′ at low frequencies are owing to charge accumulation at the prepared films and the permanent dipoles having enough time to rotate in the applied field´s direction, respectively [42]. It can be seen that after a certain critical frequency, ε′ values start to drop eventually reaching constant values at a higher frequency. This is due to the lack of ion diffusion, which prevents dipole molecules from orienting themselves in the direction of the applied electric field at high frequencies, resulting in no interfacial polarization (IP) [43]. Similar effect was found by Makled et al. for PVA/ copper iodide (CuI) polymer composite [44].

By observing the variation of ε' with T, it was found that the ε′ values gradually increase with temperature over the entire range of frequencies of the applied electric field. The behavior of ε′ with temperature can be interpreted as follows: at lower temperatures, the thermal energy absorbed by the polymeric film is low and the dipoles remain frozen and unable to respond to the applied electric field, resulting in a low dielectric constant. Furthermore, as the temperature

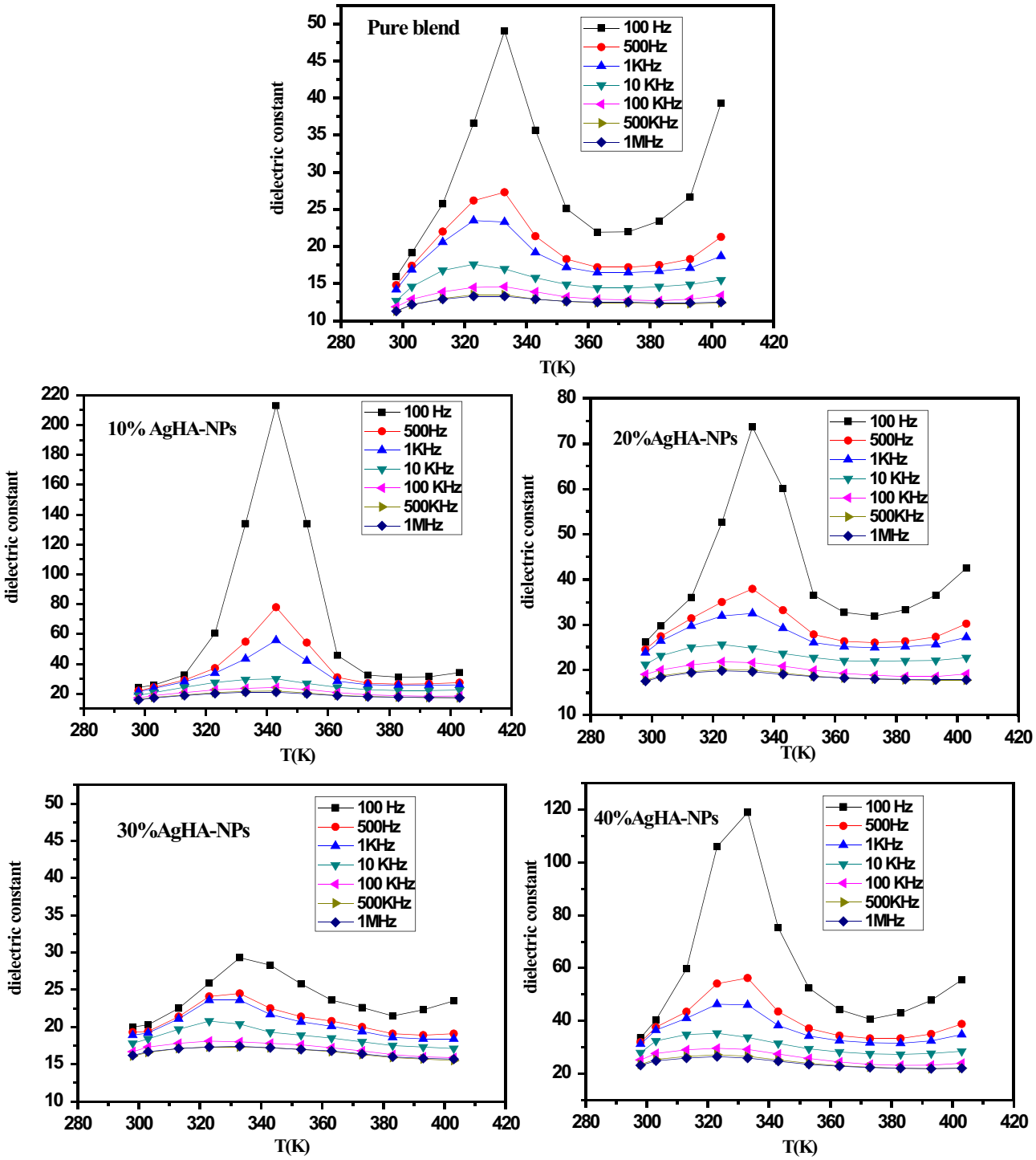

Fig. 11 Dielectric constant as a function of temperature of PVA/CMC blend, and blend loaded with (10, 20, 30, 40 wt.%) AgHA NPs

rises, the viscosity of polymeric films decreases and the dipoles have a sufficient energy to efficiently orient themselves in the direction of the applied electric field, causing the gradual increase of ε′ with temperature up to 333 K according to the free volume theory [45]. Also, it can be observed that ε′ increases with T till reach a definite value (i.e., 333 K) then decreases after (T > 343 K) according to the film composition. This behavior of ε′ could be explained as follows: when the temperature rises more than a certain value, the PVA/CMC crystalline phase starts to melt, trying to trasform from a semi-crystalline phase to the flow region. Hence, the dielectric permittivity will decrease when the

contacts between the AgHA-NPs and the polymer matrix will diminish [46]. Similar findings were also published for Co_3O_4/(CMC + PVA) nanocomposite film [47].

Figure 12 displays the temperature dependence of ε′ for PVA/CMC polymer blend doped with different concentrations of AgHA-NPs at some selected frequencies. At lower

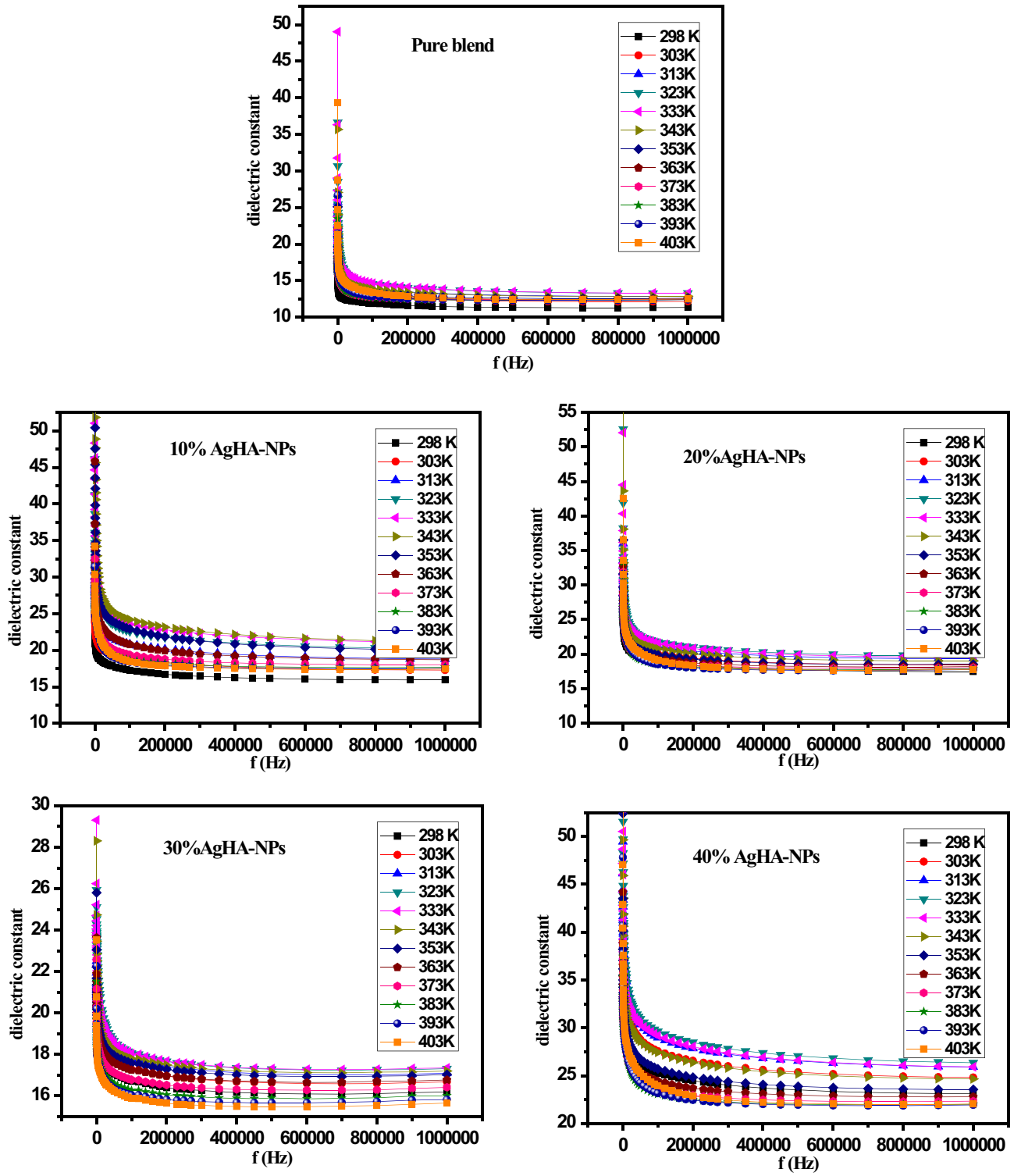

Fig. 12 The dependence of the dielectric constant on the applied frequency for PVA/CMC blend, and blend loaded with (10, 20, 30, 40 wt.%) AgHA NPs

T (≤ 320 K), the ε′ values are considered to be constant indicating that the thermal energy absorbed by PVA/CMC blend at a fixed frequency, is small and can't influence the motion of the polymer chains. On the other hand, temperature increment improves the chain mobility of the polymer system causing ε′ to increase linearly until it reaches a maximum (peak) value after which it decreases with T. Besides the IP at Ag HA-NPs and PVA/CMC interfaces, ε′ exhibits extremely significant values at lower frequencies, which can be attributed to the free charge motion inside the polymer and to the motion of polar groups [48]. However, at the high values of applied frequencies, ε′ is small and remains constant due to the polarized orientation and chain motion cannot keep up with the quickly oscillating electric field.

It is also reported that, in the studied frequency range, ε′ has higher values in all nanocomposites films than the pure blend. At room temperature (RT = 303 K), the dielectric constant ε′ increased with an increase of Ag HA-NPs percentage till 40 wt. % (ε′ = 40.3 at 100 Hz) and reduces at higher frequencies (ε′ = 24.8 at 1 MHz) but remains higher than that of pure blend (ε′ = 19.13 at 100 Hz). The SEM graphs strongly support the enhanced dielectric constant due to the improved effective interaction between the polymer matrix and the incorporated NPs as a result of their uniform dispersion, separation, and distribution all through the matrix.

AC conductivity and conduction mechanism evaluation

Figure 13 illustrates the calculated AC conductivity, $ln(\sigma_{ac})$, as a function of the reciprocal of temperature (10,000/T) for the un-filled and AgHA filled PVA/CMC films. It is obvious that σ_{ac} of each polymeric film increases with the frequency increment. It is worth noting that the value of σ_{ac} of PVA/CMC blend at RT and 1 kHz is 8.81×10^{-8} Ω^{-1} $m^{-1}$and its conductivity increases greatly by adding 40 wt.% AgHA-NPs up to 1.84×10^{-7} Ω^{-1} m^{-1}. The $\ln(\sigma_{ac})$ vs. (10,000/T) curves can be divided into two obvious regions (I and II) both of which exhibit Arrhenius behavior with high rate of conductivity increase in region I and a retreating conductivity with increasing temperature in region II. This behavior is identical to that of ε′ with T, as already discussed in a prior section. As shown in this figure, for the tested samples, σ_{ac} grows nonlinearly with temperature and the change of σ_{ac} becomes more significant at higher temperatures. This implies that σ_{ac} is a thermally induced process originating from various localized states in the band gap. As the temperature increases, the polymer chains take an easy path to transport segments that give ion migration channels resulting in an increase in the ac conductivity σ_{ac} [49]. Also, when the content of AgHA-NPs reaches to 40.0 wt. %, the values of σ_{ac} increases which is consistent with the decrease of the E_g values. The remarkable small value of E_g of (AgHA- NPs ~ 5.26 eV) may promote the growth of new energy levels in the energy band gap of the blend, creating an increase in σ_{ac} by charge carriers hopping from semi-conducting clusters to neighbors. Similar findings were obtained for PbO/CMC/PVP [50].

The ac electrical conductivity $\sigma_{ac}(\omega)$ values of PVA/CMC blend and their nanocomposites films can be calculated using the equation [51] $\sigma_{ac} = 2\pi f \varepsilon_0 \varepsilon''$. The real part of the AC conductivity, $\sigma(w)$, is obtained by the formula: $\sigma(w) = B\omega^s$, where B is constant depend on temperature and s is the frequency exponent.

Figure 14 shows the dependence of the conductivity logarithm $ln\sigma(w)$ of PVA/CMC polymeric blend and their nanocomposites filled with various concentrations of AgHA-NPs on the applied frequency lnw, at different temperatures. As seen $\sigma(w)$ of the studied samples increased almost linearly with increasing temperature, AgHA-NPs doping and frequency. The calculated values of $\sigma(w)$ at (RT = 303 K) and frequencies of 1.0 kHz, 10.0 kHz, and 1.0 MHz are recorded in Table 2. We can notice that the conductivity of PVA/CMC polymeric films is in the range from 8.81×10^{-8} Ω^{-1} m^{-1} to 4.61×10^{-5} Ω^{-1} m^{-1}. By raising the temperature up to 403 K, these values increased from 6.03×10^{-7} Ω^{-1} m^{-1} to 3.67×10^{-5} Ω^{-1} m^{-1}. Regarding to the PVA/CMC nanocomposites films, addition of AgHA-NPs slightly enhanced $\sigma(w)$ values at small temperatures, as shown in Fig. 14a–e and Table 2. Despites at T = 403 k, 40 wt.% AgHA-NPs samples show conductivity in the range from 5.05×10^{-7} Ω^{-1} m^{-1} to 6.61×10^{-5} Ω^{-1} m^{-1} which is high as compared to their values at RT. In general, introducing AgHA-NPs and/or raising the frequency and T increases the number and mobility of the charge carriers inside the polymeric blend and its nanocomposites films, resulting in higher AC conductivity values.

The dependence of frequency exponent s on the temperature can aid in explaining the dominant type of ac conduction mechanism in materials when ac electric field is applied. The conduction processes in materials under the influence of alternating field were found to match with one of the following models: (i) the quantum mechanism tunneling (QMT), (ii) the correlated barrier hopping (CBH) model [52]. According to QMT model, the power s is either increasing function of temperature or independent on temperature. Otherwise, according to CBH model, the power s decreases as temperature increases. Based on the equation $\sigma(w) = B\omega^s$, the plot of $Ln\sigma(w)vs.Ln(w)$ produces a series of straight lines with varying slopes (i.e., s values). The values of s were estimated using the plots in Fig. 14, which was then graphed as a function of T, as shown in Fig. 15. It is clear that, when the temperature rises, the s exponent for pure blend and PVA/CMC/AgHA films decreases and their values are less than unity, i.e., $0.6 < s < 1$. Findings from this study, the correlated barrier hopping (CBH) appears to be the most appropriate mechanisms for the electric conduction

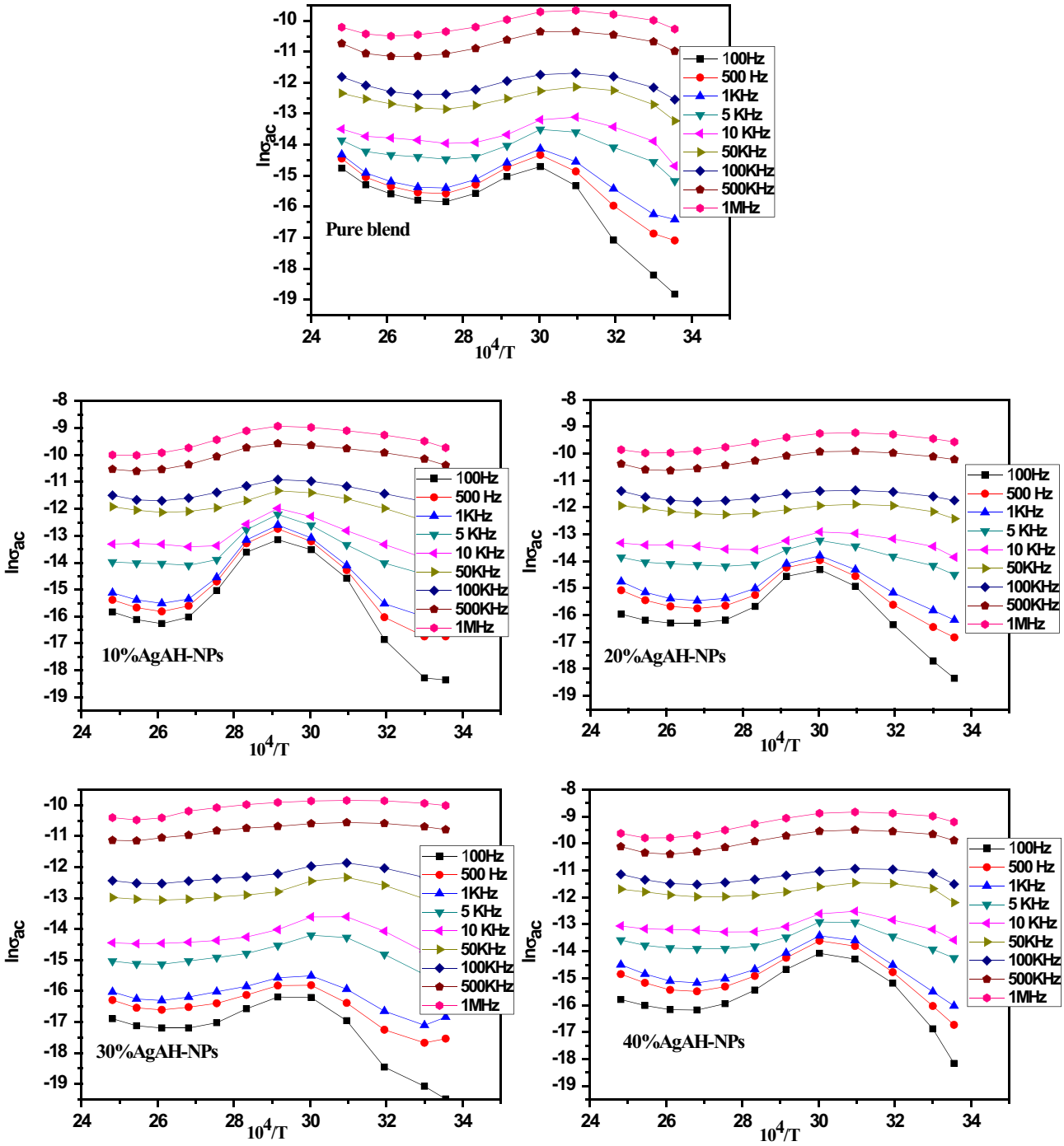

Fig. 13 The dependence of the conductivity ($ln(\sigma_{ac})$) on (10,000/ T) for PVA/CMC blend, and blend loaded with (10, 20, 30, 40 wt.%) AgHA NPs

in the blend and the blend doped with AgHA-NPs. In CBH model, the charge carrier jumps between the sites overcoming the potential barrier that separates them. As a result, one can consider that the AC conduction might be considered a thermally stimulated process. A similar outcome was recorded in the case of CMC /PVA and PVA–H_3PO_4 films [47, 53].

Evaluation of silver ion release

The silver ion releasing from the samples doped with AgHA-NPs (10, 20, 30, 40 wt.%) was investigated to clarify the results of the antimicrobial tests. Figure 16 shows the concentration of silver ion released from the prepared samples after 24 h from the incubation in phosphate buffer

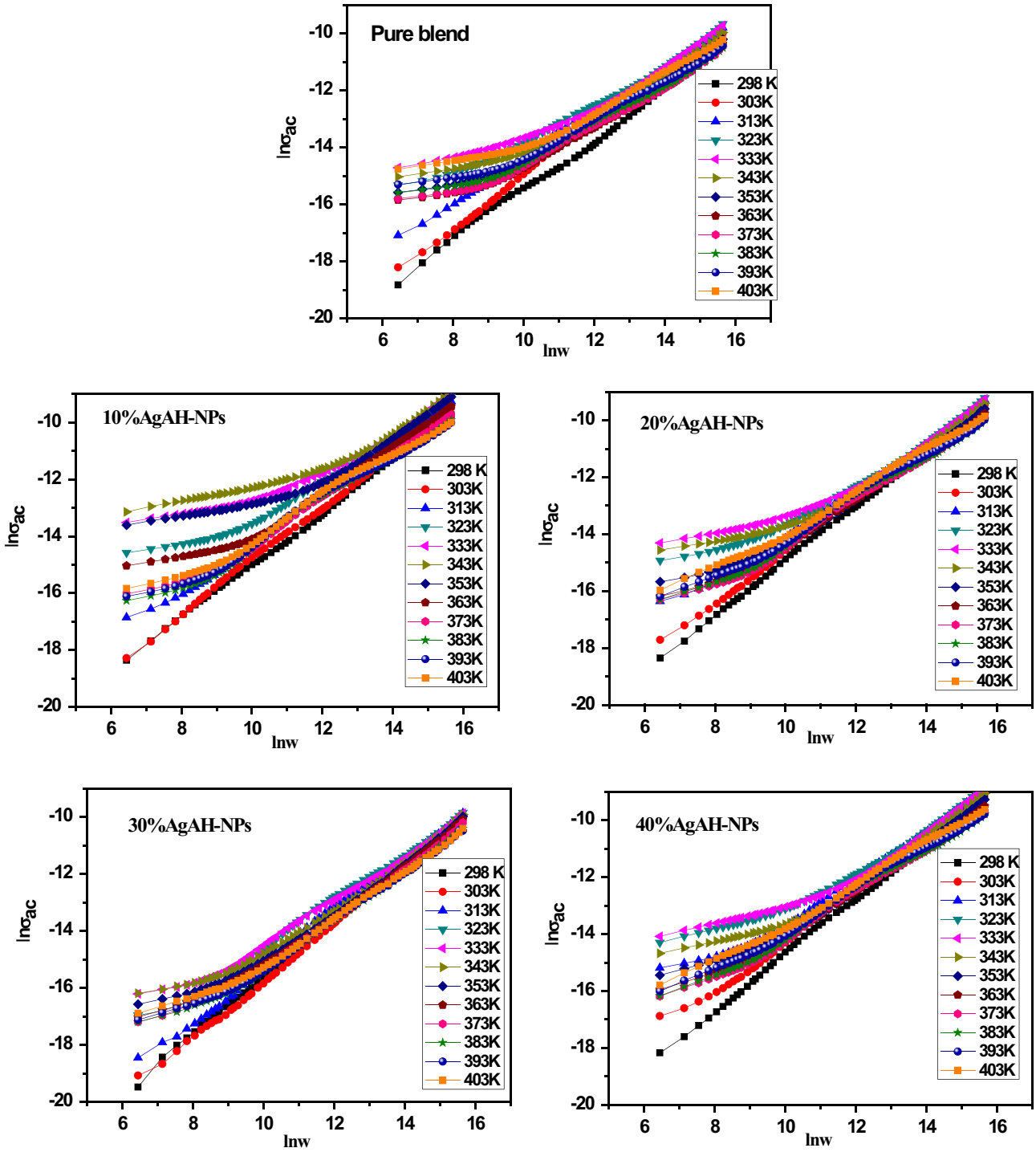

Fig. 14 AC conductivity ($ln\sigma_{ac}$)*vs*.$ln(w)$ of PVA/CMC blend, and blend loaded with (10, 20, 30, 40 wt.%) AgHA-NPs

solution. As the results indicated, the film loaded with 10 wt.% AgHA-NPs showed a small release of silver ion which amount to 0.0667 ± 0.005 mg/L and the amount of the Ag^+ released from the samples increased slowly with increasing the content of AgHA-NPs. The amount of Ag^+ released from samples loaded with AgHA-NPs (20, 30 and 40 wt.%) was 0.1146 ± 0.004 mg/L, 0.1193 ± 0.006 mg/LA and 0.1286 ± 0.007 mg/L, respectively. The release of Ag^+ should be first detached from the HA-NPs and then be released from the PVA/CMC matrix. Subsequently, a significant amount of Ag^+ was released within 24 h, which might result a strong antibacterial effect. Another mechanism is

Table 2 the AC conductivity Ω^{-1} m^{-1} (at RT = 303 K) and at different frequencies for pure blend PVA/CMC sample and its filled samples with different concentrations of AgHA-NPs

PVA/CMC blend loaded with AgHA-NPs (wt.%)	Frequency		
	1 kHz	10 kHz	1 MHz
0	8.81×10^{-8}	9.28×10^{-7}	4.61×10^{-5}
10	1.11×10^{-7}	9.83×10^{-7}	7.59×10^{-5}
20	1.33×10^{-7}	1.43×10^{-6}	7.89×10^{-5}
30	3.72×10^{-8}	3.98×10^{-7}	4.82×10^{-5}
40	1.84×10^{-7}	1.87×10^{-6}	1.25×10^{-4}

that a part of Ag^+ diffused into the solution along with the degradation of PVA/CMC and HA-NPs.

Antimicrobial activity of the PVA/CMC/AgHA nanocomposite films

Antimicrobial activities of the prepared samples were examined against microorganisms that potentially cause implant related infections [54]. The antimicrobial activity test of PVA/ CMC blend and blend doped with different concentrations of AgHA-NPs was done against gram positive (*Bacillus subtilis*) bacteria, Gram negative (*Escherichia coli*) bacteria and (*Candida albicans*) fungus. The diameter of the inhibition zone in mm was used to evaluate the antimicrobial activity of samples as shown in Fig. 17. The pure PVA/CMC films did not display an anti-bacterial effect (no zone of inhibition) toward (E. coli), but showed inhibitory index against (Bacillus subtilis) bacteria and (Candida albicans) fungus. The results illustrated that the antimicrobial activity increased with increasing the concentration of the AgHA-NPs, this implies that the antimicrobial efficiency of the materials is dependent on the amount of the AgHA-NPs

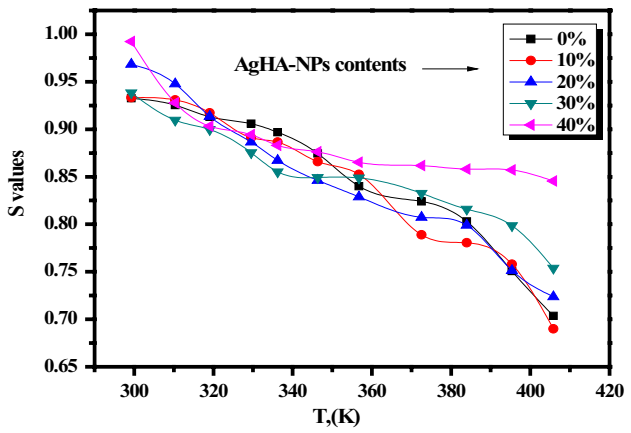

Fig. 15 The behavior of the exponent s with T (conduction mechanism evaluation) of PVA/CMC blend, and blend loaded with (10, 20, 30, 40 wt.%) AgHA NPs

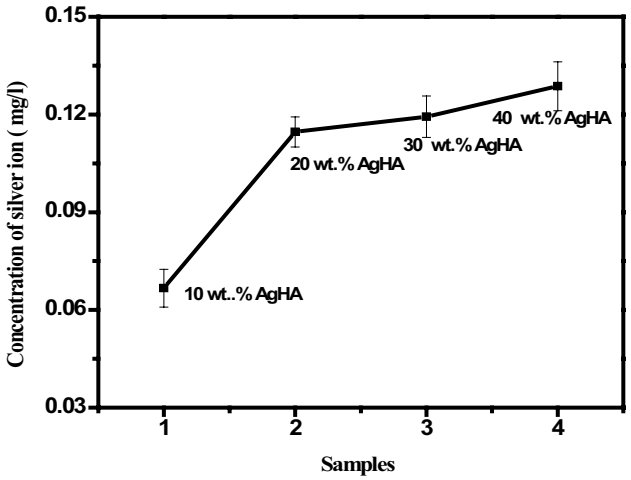

Fig. 16 Concentration of silver ion released from samples loaded with AgHA-NPs (10, 20, 30 and 40 wt.%) in phosphate buffer solution after 24 h of incubation

present. Table 3 showed the diameters of the zones of inhibition against gram positive (*Bacillus subtilis*) bacteria, Gram negative (*Escherichia coli*) bacteria and (*Candida albicans*) fungus. The antibacterial activity of hydroxyapatite is related to either Ca^{+2} alkaline earth metal ions, which according to Xie and Yang [55] are active membrane bactericide that destabilize cell membrane and kill stationary phase Staphylococcus aureus, or hydroxyl ions, which according to findings of Siqueira and Lopes [56] are highly reactive oxidant free radicals that produce a lethal effect on bacterial cells, However, the antibacterial spectrum of both Ca^{2+} and hydroxyl ions is limited.

On the other hand, for the hydroxyapatite doped with silver, the bactericidal action is thought to be caused by the release of silver (Ag^+) ions from hydroxyapatite lattice. Silver is an antibacterial agent with a broad spectrum of action [4]. According to Iqbal et al. [57] and Mocanu et al. [58], Ag^+ ions interact with bacteria´s protein and enzymes,causing structural damage of the cell membrane and of bacterial cell death. Ag^+ ion also disrupt bacteria reproduction by penetrating the cell membrane, binding to bacteria DNA and inhibiting bacterial replication.

Based on the data presented in Table 3, the samples interact with the microbial targets in distinct ways. *Bacillus subtilis* is slightly more sensitive to all samples than E. coli. One probable explanation for the differential in susceptibility between E. coli (Gram-negative) and *Bacillus subtilis* (Gram-positive) bacteria is the thickness and structure of their cell wall [59]. In case of C. albicans, all of the samples showed extremely strong antimicrobial effects. The inhibition zone of the (C. albicans) fungus did not alter significantly between the concentrations (30 and 40 wt.%),

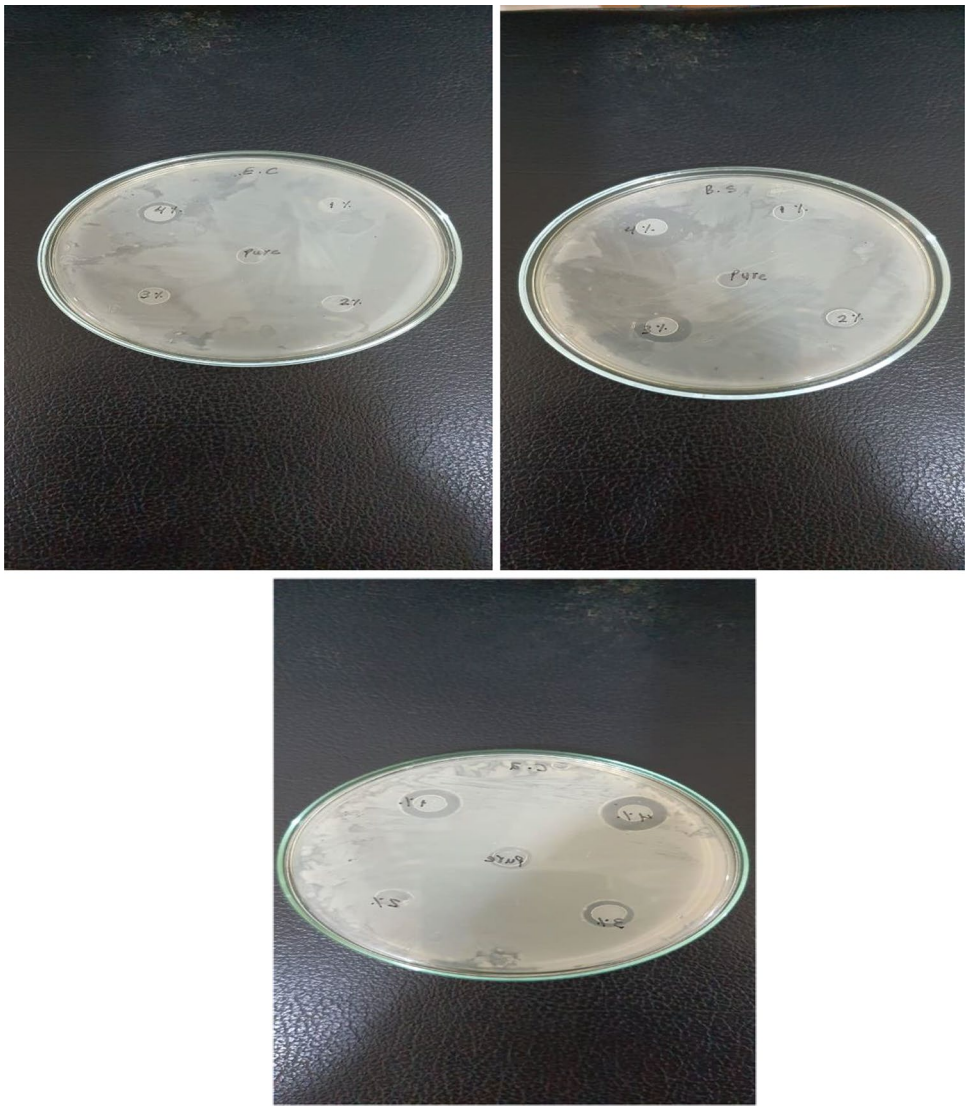

Fig. 17 The antimicrobial performance of PVA/CMC blend and the nanocomposite film against *Escherichia coli*, *Bacillus subtilis* and *Candida albicans*, where 1, 2, 3, 4% refer to (10, 20, 30, 40 wt.%) AgHA NPs

showing that (C. albicans) is not as sensitive to variations in the concentration of AgHA-NPs. These results showed that PVA/CMC/AgHA nanocomposite films had good antibacterial activity against gram positive *Bacillus subtilis* and gram negative *E.coli*, implying that they might be used in food packaging and wound dressing applications.

Table 3 Diameter of inhibition zone (mm) and percentage activity index of the prepared samples against different microorganisms (E. coli, Bacillus subtilis and C. albicans)

PVA/CMC blend loaded with AgHA-NPs (wt.%)	*E. coli*		*Bacillus subtilis*		*C. Albicans*	
	Diameter of inhibition zone (mm)	% Activity index	Diameter of inhibition zone (mm)	% Activity index	Diameter of inhibition zone (mm)	% Activity index
0	NA	—	3	13.0	7	25.9
10	NA	—	4	17.4	10	37.0
20	3	11.5	6	26.1	5	18.5
30	5	19.2	10	43.5	8	29.6
40	8	30.8	12	52.2	14	51.8

Conclusions

The AgHA-NPs have been successfully synthesized and embedded at various contents (10, 20,30 and 40 wt. %) in PVA/CMC blend. A system of PVA/CMC/AgHA nanocomposite films were prepared via the solution casting method and characterized by different techniques. This study shows that AgHA-NPs significantly affected the microstructure, optical, electrical and antimicrobial properties of nanocomposite films. XRD patterns of virgin blend and blend filled with different amounts of AgHA-NPs have a broad peak around $2\theta = 20°$ which attributed to the amorphous nature of the PVA and CMC and FTIR confirmed that AgHA-NPs stimulated the formation of intermolecular hydrogen bonds between PVA and CMC. SEM images indicated the miscibility of PVA and CMC components (in the blend) by a uniform and homogeneous smooth surface. Moreover, the surface morphology of PVA/CMC blend is dependent on the AgHA-NPs loading ratio. The optical properties for PVA/CMC/AgHA nanocomposites revealed that when the amounts AgHA-NPs in the blend increases, the absorbance, absorption coefficient, refractive index and extinction coefficient of PVA/CMC blend rise, while the transmittance and optical band gap decreased. Studying the dielectric constant proved its dependence on the frequency as well as temperature. The ac conductivity and frequency exponent s of PVA/CMC blend and their nanocomposites are found to obey the correlated barrier hopping model (CBH). The silver ion releasing from the samples doped with AgHA-NPs (10, 20, 30, 40 wt.%) increased slowly with increasing the content of AgHA-NPs. A significant improvement in antimicrobial activity of films against gram positive *(Bacillus subtilis)*, gram-negative *(Escherichia coli)* bacteria and fungi (*Candida albicans*) was obtained by raising the content of AgHA-NPs suggested that the incorporation of silver doped hydroxyapatite nanoparticles AgHA-NPs into PVA/CMC can be used in many antimicrobial application.

Funding Open access funding provided by The Science, Technology & Innovation Funding Authority (STDF) in cooperation with The Egyptian Knowledge Bank (EKB).

Declarations

Competing interest The authors declare that they have no known competing financial interests or personal relationships that could have appeared to influence the work reported in this paper.

References

1. He S, Wang J, Yu M, Xue Y, Hu J, Lin J (2019) Structure and Mechanical Performance of Poly(vinyl Alcohol) Nanocomposite by incorporating graphitic carbon nitride nanosheets. Polymers 11:610
2. Nihmath A, Ramesan MT (2017) Fabrication. Characterization and dielectric studies of NBR/ hydroxyapatite nanocomposites. J Inorg Organomet Polym 27:481–489
3. Tamayo L, Azócar M, Kogan M, Riveros A, Páez M (2016) Copper-polymer nanocomposites: An excellent and cost-effective biocide for use on antibacterial surfaces, 2016. Mater Sci Eng C 69:1391–1409
4. Ciobanu SC, Iconaru LS, Chifiriuc CM, Costescu A, Coustumer LP, Predoi D (2013) Synthesis and antimicrobial activity of silver-doped hydroxyapatite nanoparticles. Biomed Res Int 2013:1–10
5. Pandele AM, Constantinescu A, Radu IC, Miculescu F, Voicu SI, Ciocan LT (2020) Synthesis and characterization of PLA-micro-structured hydroxyapatite composite films. Materials 13:274
6. Alshemary AZ, Akram M, Goh YF, Kadir MRA, Abdolahi A, Hussain R (2015) Structural characterization, optical properties and in vitro bioactivity of mesoporous erbium-doped hydroxyapatite. J Alloy Compd 645:478–486
7. Gopi D, Ramya S, Rajeswari D, Karthikeyan P, Kavitha L (2014) Strontium, cerium co-substituted hydroxyapatite nanoparticles: synthesis, characterization, antibacterial activity towards prokaryotic strains and in vitro studies. Colloids Surf A Physicochem Eng Aspects 451:172–180
8. Li Y, Ooi CP, Hong Ning PC, Khor KA (2009) Synthesis and characterization of neodymium(III) and gadolinium(III)-substituted hydroxyapatite as biomaterials. Int J Appl Ceram Technol 6:501–512
9. André RS, Paris EC, Gurgel MFC, Rosa ILV, Paiva-Santos CO, Li MS, Varela JA, Longo E (2012) Structural evolution of Eu-doped hydroxyapatite nanorods monitored by photoluminescence emission. J Alloys Comp 531:50–54
10. Ciobanu CS, Iconaru SL, Pasuk I, Vasile BS, Lupu AR, Hermenean A, Dinischiotu A, Predoi D (2013) Structural properties of silver doped hydroxyapatite and their biocompatibility. Mater Sci Eng C Mater 33:1395–1402
11. Cinteza LO, Scomoroscenco C, Voicu SN, Nistor CL, Nitu SG, Trica B, Jecu M-L, Petcu C (2018) Chitosan-stabilized Ag nanoparticles with superior biocompatibility and their synergistic antibacterial effect in mixtures with essential oils. Nanomaterials (Basel) 8:826
12. Jain J, Arora S, Rajwade JM, Omray P, Khandelwal S, Paknikar KM (2009) Silver nanoparticles in therapeutics: development of an antimicrobial gel formulation for topical use. Mol Pharm 6:1388–1401
13. Maneerung T, Tokura S, Rujiravanit R (2008) Impregnation of silver nanoparticles into bacterial cellulose for antimicrobial wound dressing. Carbohyd Polym 72:43–51
14. Chaloupka K, Malam Y, Seifalian AM (2010) Nanosilver as a new generation of nanoproduct in biomedical applications. Trends Biotechnol 28:580–588
15. Song JL, Birbach NL, Hinestroza JP (2012) Deposition of silver nanoparticles on cellulosic fibers via stabilization of carboxymethyl groups. Cellulose 19:411–424
16. Morsi MA, Hezma AM (2019) Effect of iron doped hydroxyapatite nanoparticles on the structural, morphological, mechanical

and magnetic properties of polylactic acid polymer. J Market Res 8:2098–2106
17. Morsi MA, Oraby AH, Elshahawy AG, Abd El Hady RM (2019) Preparation, structural analysis, morphological investigation and electrical properties of gold nanoparticles filled polyvinyl alcohol/carboxymethyl cellulose blend. J Market Res 8:5996–6010
18. El Fewaty NH, El Sayed AM, Hafez RS (2016) Synthesis, structural and optical properties of tin oxide nanoparticles and its CMC/PEG–PVA nanocomposite films. Polym Sci Ser A 58:1004–1016
19. Hashim A, Hadi Q (2018) Structural, electrical and optical properties of (biopolymer blend/titanium carbide) nanocomposites for low cost humidity sensors. J Mater Sci Mater Electron 29:11598–11604
20. El-Sayed S, Mahmoud KH, Fatah AA, Hassen A (2011) DSC, TGA and dielectric properties of carboxymethyl cellulose/polyvinyl alcohol blends. Physica B 406:4068–4076
21. Zhu J, Li Q, Che Y, Liu X, Dong C, Chen X, Wang C (2020) Effect of Na_2CO_3 on the microstructure and macroscopic properties and mechanism analysis of PVA/CMC composite film. Polymers 12:453–465
22. Alghunaim NS (2019) Effect of CuO nanofiller on the spectroscopic properties, dielectric permittivity and dielectric modulus of CMC/PVP nanocomposites. J Market Res 8:3596–3602
23. Riaz M, Zia R, Saleemi F, Hussain T, Bashir F, Ikhram H (2016) Effect of Ti^{+4} on in vitro bioactivity and antibacterial activity of silicate glass-ceramics. Mater Sci Eng C 69:1058–1067
24. Ravindran A, Singh A, Raichur AM, Chandrasekaran N, Mukherjee A (2010) Studies on interaction of colloidal Ag nanoparticles with bovine serum albumin (BSA). Colloids Surf B 76:32–37
25. Ren F, Xin R, Ge X, Leng Y (2009) Characterization and structural analysis of zinc substituted hydroxyapatites. Acta Biomater 5:3141–3149
26. Saadiah MA, Zhang D, Nagao Y, Muzakir SK, Samsudin AS (2019) reducing crystallinity on thin film based CMC/PVA hybrid polymer for application as a host in polymer electrolytes. J Non-Cryst Solids 511:201–211
27. Hema M, Selvasekerapandian S, Sakunthala A, Arunkumar D, Nithya H (2008) Structural, vibrational and electrical characterization of PVA–NH_4Br polymer electrolyte system. Physica B 403:2740–2747
28. Menazea AA, Awwad NS, Ibrahiumd HA, Ahmed MK (2020) Casted polymeric blends of carboxymethyl cellulose/polyvinyl alcohol doped with gold nanoparticles via pulsed laser ablation technique; morphological features, optical and electrical investigation. Rad Phys Chem 177:109155
29. Bastan FE (2020) Fabrication and characterization of an electrostatically bonded PEEK- hydroxyapatite composites for biomedical applications. J Biomed Mater Res Part B 108:2513–2527
30. Han JH, Floros JD (1997) Casting antimicrobial packaging films and measuring their physical properties and antimicrobial activity. J Plast Film Sheeting 13:287–298
31. El Sayed AM, El-Gamal S, Morsi WM, Mohammed Gh (2015) Effect of PVA and copper oxide nanoparticles on the structural, optical, and electrical properties of carboxymethyl cellulose films. J Mater Sci 50:4717–4728
32. Fasihia H, Fazilatia M, Hashemic M, Noshirvani N (2017) Novel carboxymethyl cellulose-polyvinyl alcohol blend filmsstabilized by Pickering emulsion incorporation method. Carbohyd Polym 167:79–89
33. Abdelrazek EM, Abdelghany AM, Badr SI, Morsi MA (2018) Structural, optical, morphological and thermal properties of PEO/PVP blend containing different concentrations of biosynthesized Au nanoparticles. J Market Res 7:419–431
34. Ali FM (2020) Synthesis and Characterization of a Novel Erbium Doped Poly(vinyl alcohol) Films for multifunctional optical materials. J Inorg Organomet Polym Mater 30:2418–2429
35. Ghanipour M, Dorranian D (2013) Effect of Ag-nanoparticles doped in polyvinyl alcohol on the structural and optical properties of pva films. J Nanomater 10
36. Mott NF, Davis NF (1979) Electronic process in non-crystalline materials, 2nd edn. Oxford University Press, USA
37. Morsi MA, Abdelaziz M, Oraby AH, Mokhles I (2019) Structural, optical, thermal, and dielectric properties of polyethyleneoxide/carboxymethyl cellulose blend filled with bariumtitanate. J Phys Chem Solids 125:46–49
38. Escobar-Alarcon L, Arrieta A, Camps E, Muhl S, Rodil S, Vigueras-Santiago E (2007) An alternative procedure for the determination of the optical band gap and thickness of amorphous carbon nitride thin films. Appl Surf Sci 254:412–415
39. Aslam M, Kalyar MA, Raza ZA (2017) Graphene oxides nanosheets mediation of poly(vinyl alcohol) films in tuning their structural and opto-mechanical attributes. J Mater Sci Mater Electron 28:13401–13413
40. Abdelaziz M (2011) Cerium (III) doping effects on optical and thermal properties of PVA films. Phys B 406:1300–1307
41. Al-Attiyah KHH, Hashim A, Obaid SF (2019) Fabrication of novel (carboxy methyl cellulose–polyvinylpyrrolidone–polyvinyl alcohol)/lead oxide nanoparticles: structural and optical properties for gamma rays shielding applications. Int J Plast Technol 23:39–45
42. Abdullah OGh, Aziz SB, Rasheed MA (2018) Incorporation of NH_4NO_3 into MC-PVA blend-based polymer to prepare proton-conducting polymer electrolyte films. Ionics 24:777–785
43. Mohammed G, El Sayed AM (2019) Structural, morphological, optical and dielectric properties of M^{3+}/ PVA/PEG SPE Films (M = La, Y, Fe or Ir). Polym Adv Technol 30:698–712
44. Makled MH, Sheha E, Shanap TS, El-Mansy MK (2012) Electrical conduction and dielectric relaxation in p-type PVA/CuI polymer composite. J Adv Res 4:531–538
45. Abdel-Baset A, Hassen A (2016) Dielectric relaxation analysis and Ac conductivity of polyvinyl alcohol/polyacrylonitrile film. Physica B 499:24–28
46. El-Gamal S, El Sayed AM (2019) Physical properties of the organic polymeric blend (PVA/PAM) modified with MgO nanofillers. J Compos Mater 53:2831–2847
47. El Sayed AM, El-Gamal S (2015) Synthesis and investigation of the electrical and dielectric properties of Co_3O_4/ (CMC+PVA) nanocomposite films. J Polym Res 22:1–12
48. El-Sayed S (2014) Optical properties and dielectric relaxation of polyvinylidene fluoride thin films doped with gadolinium chloride. Physica B 454:197–203
49. Nasrallah DA, El-Metwally EG, Ismail AM (2020) Structural, thermal, and dielectric properties of porous PVDF/$Li_4Ti_5O_{12}$ nanocomposite membranes for high-power lithium-polymer batteries. Polym Adv Technol 32:1214–1229
50. El-Bana MS, Mohammed Gh, El Sayed AM, El-Gamal S (2018) Preparation and characterization of PbO/carboxymethyl cellulose/polyvinylpyrrolidone nanocomposite films. Polym Compos 39:3712–3725
51. Mohammed MI, Fouad SS, Mehta N (2018) Dielectric relaxation and thermally activated a.c. conduction in (PVDF)/(rGO) nano-omposites: role of rGO over different fillers. J Mater Sci 29:18271–18281
52. Austin IG, Mott MF (1969) Polarons in crystalline and non-crystalline materials. Adv Phys 18:41–102
53. Prajapati GK, Gupta PN (2009) Conduction mechanism in unirradiated and γ-irradiated PVA–H_3PO_4 polymer electrolytes. Nucl Instr Meth B 267:3328–3332
54. Campoccia D, Montanaro L, Arciola CR (2006) the significance of infection related to orthopedic devices and issues of antibiotic resistance. Biomaterials 27:2331–2339
55. Xie Y, Yang L (2016) Calcium and magnesium ions are membrane-active against stationary-phase Staphylococcus aureus with high specificity. Sci Rep 6:1–8

56. Siqueira JF Jr, Lopes HP (1999) Mechanisms of antimicrobial activity of calcium hydroxide: a critical review. Int Endod J 32:361–369
57. Iqbal N, Kadir MRA, Mahmood NHB, Iqbal S, Almasi D, Naghizadeh F, Kamarul T (2015) Characterization and biological evaluation of silver containing fluoroapatite nanoparticles prepared through microwave synthesis. Ceram Int 41:6470–6477
58. Mocanu A, Furtos G, Rapuntean S, Horovitz O, Flore C, Garbo C, Tomoaia-Cotisel M (2014) Synthesis; characterization and antimicrobial effects of composites based on multi-substituted hydroxyapatite and silver nanoparticles. Appl Surf Sci 298:225–235
59. Stanić V, Janaćković D, Dimitrijević S, Tanasković SB, Mitrić M, Pavlović MS, Krstić A, Jovanović D, Raičević S (2011) Synthesis of antimicrobial monophase silver-doped hydroxyapatite nanopowders for bone tissue engineering. Appl Surf Sci 257:4510–4518